

# Ultrahigh-resolution high-speed retinal imaging using spectral-domain optical coherence tomography

Barry Cense, Nader A. Nassif

Harvard Medical School and Wellman Center for Photomedicine, Massachusetts General Hospital, 50 Blossom Street, BAR 714, Boston, Massachusetts 02114  
[bcense@helix.mgh.harvard.edu](mailto:bcense@helix.mgh.harvard.edu)

Teresa C. Chen

Massachusetts Eye and Ear Infirmary and Harvard Medical School, 243 Charles Street, Boston, Massachusetts 02114

Mark C. Pierce, Seok-Hyun Yun, B. Hyle Park, Brett E. Bouma, Guillermo J. Tearney, Johannes F. de Boer

Harvard Medical School and Wellman Center for Photomedicine, Massachusetts General Hospital, 50 Blossom Street, BAR 714, Boston, Massachusetts 02114  
[deboer@helix.mgh.harvard.edu](mailto:deboer@helix.mgh.harvard.edu)

**Abstract:** We present the first ultrahigh-resolution optical coherence tomography (OCT) structural intensity images and movies of the human retina *in vivo* at 29.3 frames per second with 500 A-lines per frame. Data was acquired at a continuous rate of 29,300 spectra per second with a 98% duty cycle. Two consecutive spectra were coherently summed to improve sensitivity, resulting in an effective rate of 14,600 A-lines per second at an effective integration time of 68  $\mu$ s. The turn-key source was a combination of two super luminescent diodes with a combined spectral width of more than 150 nm providing 4.5 mW of power. The spectrometer of the spectral-domain OCT (SD-OCT) setup was centered around 885 nm with a bandwidth of 145 nm. The effective bandwidth in the eye was limited to approximately 100 nm due to increased absorption of wavelengths above 920 nm in the vitreous. Comparing the performance of our ultrahigh-resolution SD-OCT system with a conventional high-resolution time domain OCT system, the A-line rate of the spectral-domain OCT system was 59 times higher at a 5.4 dB lower sensitivity. With use of a software based dispersion compensation scheme, coherence length broadening due to dispersion mismatch between sample and reference arms was minimized. The coherence length measured from a mirror in air was equal to 4.0  $\mu$ m ( $n = 1$ ). The coherence length determined from the specular reflection of the foveal umbo *in vivo* in a healthy human eye was equal to 3.5  $\mu$ m ( $n = 1.38$ ). With this new system, two layers at the location of the retinal pigmented epithelium seem to be present, as well as small features in the inner and outer plexiform layers, which are believed to be small blood vessels.

©2004 Optical Society of America

**OCIS codes:** (170.4500) Optical Coherence Tomography (170.4470) Ophthalmology; (170.3890) Medical optics instrumentation; (110.4280) Noise in imaging systems;

---

## References and Links

1. D. Huang, E.A. Swanson, C.P. Lin, et al., "Optical coherence tomography," *Science* **254**, 1178-81 (1991).

#4033 - \$15.00 US  
(C) 2004 OSA

Received 16 March 2004; revised 17 May 2004; accepted 19 May 2004  
31 May 2004 / Vol. 12, No. 11 / OPTICS EXPRESS 2435

2. F.W. Campbell and D.G. Green, "Optical and Retinal Factors Affecting Visual Resolution," *J. Physiol.-London* **181**, 576-593 (1965).
3. E.A. Swanson, D. Huang, M.R. Hee, et al., "High-Speed Optical Coherence Domain Reflectometry," *Opt. Lett.* **17**, 151-153 (1992).
4. W. Drexler, U. Morgner, F.X. Kartner, et al., "In vivo ultrahigh-resolution optical coherence tomography," *Opt. Lett.* **24**, 1221-1223 (1999).
5. W. Drexler, H. Sattmann, B. Hermann, et al., "Enhanced visualization of macular pathology with the use of ultrahigh-resolution optical coherence tomography," *Arch. Ophthalmol.* **121**, 695-706 (2003).
6. W. Drexler, U. Morgner, R.K. Ghanta, et al., "Ultrahigh-resolution ophthalmic optical coherence tomography," *Nat. Med.* **7**, 502-507 (2001).
7. American National Standards Institute, American National Standard for Safe Use of Lasers Z136.1. 2000: Orlando.
8. C.K. Hitzenberger, P. Trost, P.W. Lo and Q.Y. Zhou, "Three-dimensional imaging of the human retina by high-speed optical coherence tomography," *Opt. Express* **11**, 2753-2761 (2003), <http://www.opticsexpress.org/abstract.cfm?URI=OPEX-11-21-2753>
9. B. Cense, T.C. Chen, B.H. Park, M.C. Pierce and J.F. de Boer, "In vivo depth-resolved birefringence measurements of the human retinal nerve fiber layer by polarization-sensitive optical coherence tomography," *Opt. Lett.* **27**, 1610-1612 (2002).
10. B. Cense, T.C. Chen, B.H. Park, M.C. Pierce and J.F. de Boer, "In vivo birefringence and thickness measurements of the human retinal nerve fiber layer using polarization-sensitive optical coherence tomography," *J. Biomed. Opt.* **9**, 121-125 (2004).
11. A.F. Fercher, C.K. Hitzenberger, G. Kamp and S.Y. Elzaiat, "Measurement of Intraocular Distances by Backscattering Spectral Interferometry," *Opt. Commun.* **117**, 43-48 (1995).
12. G. Hausler and M.W. Lindner, "Coherence Radar and Spectral Radar - new tools for dermatological diagnosis," *J. Biomed. Opt.* **3**, 21-31 (1998).
13. A.F. Fercher, W. Drexler, C.K. Hitzenberger and T. Lasser, "Optical coherence tomography - principles and applications," *Rep. Prog. Phys.* **66**, 239-303 (2003).
14. T. Mitsui, "Dynamic range of optical reflectometry with spectral interferometry," *Jpn. J. Appl. Phys. Part 1 - Regul. Pap. Short Notes Rev. Pap.* **38**, 6133-6137 (1999).
15. R. Leitgeb, C.K. Hitzenberger and A.F. Fercher, "Performance of fourier domain vs. time domain optical coherence tomography," *Opt. Express* **11**, 889-894 (2003), <http://www.opticsexpress.org/abstract.cfm?URI=OPEX-11-8-889>
16. J.F. de Boer, B. Cense, B.H. Park, et al., "Improved signal-to-noise ratio in spectral-domain compared with time-domain optical coherence tomography," *Opt. Lett.* **28**, 2067-2069 (2003).
17. M.A. Choma, M.V. Sarunic, C.H. Yang and J.A. Izatt, "Sensitivity advantage of swept source and Fourier domain optical coherence tomography," *Opt. Express* **11**, 2183-2189 (2003), <http://www.opticsexpress.org/abstract.cfm?URI=OPEX-11-18-2183>
18. N. Nassif, B. Cense, B.H. Park, et al., "In vivo human retinal imaging by ultrahigh-speed spectral domain optical coherence tomography," *Opt. Lett.* **29**, 480-482 (2004).
19. M. Wojtkowski, R. Leitgeb, A. Kowalczyk, T. Bajraszewski and A.F. Fercher, "In vivo human retinal imaging by Fourier domain optical coherence tomography," *J. Biomed. Opt.* **7**, 457-463 (2002).
20. N.A. Nassif, B. Cense, B.H. Park, et al., "In vivo high-resolution video-rate spectral-domain optical coherence tomography of the human retina and optic nerve," *Opt. Express* **12**, 367-376 (2004), <http://www.opticsexpress.org/abstract.cfm?URI=OPEX-11-7-782>
21. G.J. Tearney, B.E. Bouma and J.G. Fujimoto, "High-speed phase- and group-delay scanning with a grating-based phase control delay line," *Opt. Lett.* **22**, 1811-1813 (1997).
22. J.F. de Boer, C.E. Saxer and J.S. Nelson, "Stable carrier generation and phase-resolved digital data processing in optical coherence tomography," *Appl. Opt.* **40**, (2001).
23. A.F. Fercher, C.K. Hitzenberger, M. Sticker, et al., "Dispersion compensation for optical coherence tomography depth-scan signals by a numerical technique," *Opt. Commun.* **204**, 67-74 (2002).
24. D.L. Marks, A.L. Oldenburg, J.J. Reynolds and S.A. Boppart, "Digital algorithm for dispersion correction in optical coherence tomography for homogeneous and stratified media," *Appl. Opt.* **42**, 204-217 (2003).
25. D.L. Marks, A.L. Oldenburg, J.J. Reynolds and S.A. Boppart, "Autofocus algorithm for dispersion correction in optical coherence tomography," *Appl. Opt.* **42**, 3038-3046 (2003).
26. S.H. Yun, G.J. Tearney, B.E. Bouma, B.H. Park and J.F. de Boer, "High-speed spectral-domain optical coherence tomography at 1.3  $\mu$  m wavelength," *Opt. Express* **11**, 3598-3604 (2003), <http://www.opticsexpress.org/abstract.cfm?URI=OPEX-11-26-3598>
27. B.R. White, M.C. Pierce, N. Nassif, et al., "In vivo dynamic human retinal blood flow imaging using ultra-high-speed spectral domain optical Doppler tomography," *Opt. Express* **11**, 3490-3497 (2004), <http://www.opticsexpress.org/abstract.cfm?URI=OPEX-11-25-3490>
28. D.M. Snodderly, R.S. Weinhaus and J.C. Choi, "Neural Vascular Relationships in Central Retina of Macaque Monkeys (*Macaca-Fascicularis*)," *J. Neurosci.* **12**, 1169-1193 (1992).

## 1. Introduction

The time-domain variant of optical coherence tomography [1] (TD-OCT) is a technique that is clinically applied in ophthalmology for the detection of ocular diseases, as well as for monitoring of disease progression and the effects of therapy. Based on interferometry with near infrared light, TD-OCT allows for non-invasive and *in vivo* optical cross-sectioning of the retina and cornea. Since it is not possible to take a biopsy of the retina on a routine basis, TD-OCT is one of the few tools available for ophthalmologists to obtain depth-resolved retinal information.

Compared to histology, one drawback of TD-OCT is its limited lateral and axial resolution. The lateral resolution of the technique is limited by the optics of the eye, i.e. the focal length, corneal aberrations and pupil diameter, [2] and the optical design of the setup. Without adaptive optics, the combination of these parameters leads to a lateral resolution of approximately 20-30  $\mu\text{m}$ . The axial resolution of an OCT system may be defined in terms of the coherence length,  $l_{coh}$ , which is determined by the center wavelength and bandwidth of the source and the index of refraction of the medium.[3]

*In vivo* OCT measurements of an African frog tadpole with an axial resolution of  $\sim 1 \mu\text{m}$  can be made using a Ti:sapphire laser with a bandwidth of 350 nm centered around 800 nm. [4] Drexler *et al* obtained retinal images with an axial resolution of 3  $\mu\text{m}$ , [5] using a technique called ultrahigh-resolution optical coherence tomography (HR-OCT).[4-6]

The image quality or signal to noise ratio (SNR) of a shot-noise-limited TD-OCT system depends on several factors. [3] The application of a source with a larger bandwidth decreases SNR due to the increased electronic detection bandwidth required. In order to maintain the same SNR, either A-line rate or axial scan length should be decreased, or the power incident on the sample should be increased. If the dwell time of the imaging spot on the retina is kept short, ANSI standards allow an increase of sample power. [7] Short dwell times can be achieved if the OCT beam is scanned sufficiently fast over the retina. Hitztenberger *et al* performed ophthalmic TD-OCT with short dwell times and incident power of up to 10 mW. [8] In previous measurements with our ophthalmic TD-OCT system, the power incident on the eye was less than 600  $\mu\text{W}$ , [9, 10] because this power level is known to be safe for dwell times of up to eight hours. [7] An increase in sample arm power to 10 mW could result in more than a tenfold increase in SNR. However, more source power is required and inexpensive powerful sources with a large bandwidth are not readily available. For current clinical ophthalmic applications of HR-OCT, either a lower SNR or a slower A-line rate is taken as a penalty. One can avoid such a penalty by using a more sensitive technique.

In spectral-domain optical coherence tomography (SD-OCT), also known as Fourier-domain OCT (FD-OCT), depth-resolved information is encoded in the cross-spectral density function, as measured in the detection arm of an interferometer. [11-13] SD-OCT offers a significant sensitivity advantage over TD-OCT. [14-17] Recently, in a direct comparison, an improvement of more than 2 orders of magnitude (21.7 dB) was experimentally demonstrated. [18] In addition, the reference arm length in SD-OCT is not modulated, making SD-OCT inherently faster than TD-OCT. The SNR of an SD-OCT system is defined as: [16]

$$SNR_{SD-OCT} = \frac{\eta \cdot P_{sample} \cdot \tau_i}{E_v} \quad (1)$$

with  $\tau_i$  the integration time required to record one spectrum. According to Eq. 1, the SNR performance of an SD-OCT system improves with increasing sample arm power or longer integration time. Most importantly, Eq. 1 shows that the SNR performance of an SD-OCT system is independent of the bandwidth of the source. In theory, by combining SD-OCT with an ultra-broadband source, ultrahigh-resolution imaging at high acquisition rates should become within reach. This new technique may facilitate the diagnosis and monitoring of several ocular diseases, such as glaucoma, diabetic retinopathy, cancer and age-related

macular degeneration. The first *in vivo* retinal SD-OCT images were presented by Wojtkowski *et al.*[19] In our previous work, we demonstrated an SD-OCT system suitable for *in vivo* video-rate ophthalmic imaging. [18, 20] This system had a sensitivity of 98.4 dB, an acquisition rate of 29,300 A-lines per second and an axial resolution of 6  $\mu\text{m}$  in the eye at a safe ocular exposure level of 600  $\mu\text{W}$ . Motion artifacts within a frame due to involuntary eye movement were avoided at this frame rate. Furthermore, three-dimensional tomograms were created, which represent the true topography of the retina. In this paper we will quantify the signal to noise ratio (SNR) and the axial resolution of an SD-OCT system equipped with an ultra-broadband source and identify not earlier seen features in the retina.

One difficulty that arises from using ultra-broadband sources in a fiber-based OCT setup for ophthalmic imaging is chromatic dispersion in optically-dense materials like glass, tissue and water. The speed of light depends on the refractive index  $n(k)$  of the material, slowing down certain spectral components to a greater extent than others, hence dispersing the light. The total amount of dispersion increases linearly with length of the dispersive medium as well. Chromatic dispersion in air is negligible. Considerable amounts of dispersion can be tolerated if the dispersion in the two arms of the interferometer is equal, thus creating a coherence function that will be free of dispersion artifacts. However, when sample and reference arms contain different lengths of optical fiber or other dispersive media, a dispersion mismatch occurs. In the sample arm, the introduction of an eye with unknown axial length creates a similar effect. The coherence function will not only be broadened by unbalanced dispersion, but its peak intensity will decrease as well. Second order or group-velocity dispersion can be compensated for by changing the lens to grating distance in a rapid scanning optical delay line. [21] However, this method does not compensate for higher orders of dispersion. Alternatively, one can balance dispersion in an OCT system by inserting variable-thickness BK7 and fused silica prisms in the reference arm. [4] The previously-mentioned unknown factor introduced by an eye with unknown axial length requires a flexible method for dispersion compensation. An alternative to compensation in hardware is dispersion compensation in software. De Boer *et al* induced dispersion in the delay line of a TD-OCT system equipped with an optical amplifier based source (AFC technologies,  $\lambda_0 = 1310 \text{ nm}$ ,  $\Delta\lambda = 75 \text{ nm}$ ) and compensated for dispersion artifacts in structural intensity images obtained in an onion. [22] Fercher *et al* compensated for dispersion induced by a glass sample. [23] Their broadband spectrum was generated with a high-pressure mercury lamp. Other dispersion compensation algorithms are described by Marks *et al.* [24, 25] In our analysis we will compensate in software for dispersion induced by an ultra-broadband source and remove artifacts from retina data. For the near future, this technology may facilitate the application of ultrahigh-resolution systems in the clinic.

### 3. Method

#### 3.1 Dispersion compensation

A dispersion mismatch introduces a phase shift  $e^{i\theta(k)}$  in the complex cross-spectral density  $I(k)$  as a function of wave vector. Since spectrometer data is acquired as a function of wavelength, data has to be transformed to  $k$ -space first. The relation between the phase  $\theta(k)$  and the multiple orders of dispersion can best be described by a Taylor series expansion:

$$\theta(k) = \theta(k_0) + \left. \frac{\partial\theta(k)}{\partial k} \right|_{k_0} (k_0 - k) + \frac{1}{2} \cdot \left. \frac{\partial^2\theta(k)}{\partial k^2} \right|_{k_0} (k_0 - k)^2 + \dots + \frac{1}{n!} \cdot \left. \frac{\partial^n\theta(k)}{\partial k^n} \right|_{k_0} (k_0 - k)^n \quad (2)$$

with  $\lambda_0$  the center wavelength and  $k_0$  equal to  $2\pi/\lambda_0$ . The first two terms describe a constant offset and group velocity, respectively, and are not related to dispersive broadening. The third term represents second order or group-velocity dispersion. Dispersion mismatch in sample and reference arms is largely compensated by this term, although adjustment of higher order dispersion can be necessary as well, especially when an ultra-broadband source is used. Dispersion can be removed by multiplying the dispersed cross-spectral density function  $I(k)$

with a phase term  $e^{-i\theta(k)}$ . To determine this phase term for dispersion compensation of data obtained in the human eye *in vivo* requires a coherence function obtained from a well-reflecting reference point in the eye. We found that it is possible to use the center of the fovea (foveal umbo) for this purpose, because this part of the eye acts as a good reflector. To determine the phase term, after linear interpolation to  $k$ -space, the spectrum is Fourier transformed to  $z$ -space, where it is shifted such that the coherence function is centered on the origin. A complex spectrum in  $k$ -space is obtained after an inverse Fourier transformation. The phase term  $\theta(k)$  is equal to the arctangent of the imaginary component divided by the real component, and indicates by how much subsequent wave numbers  $k$  are out of phase with each other. This function was fit to a polynomial expression of 9<sup>th</sup> order, yielding a set of coefficients  $\alpha_{1-9}$ . Individual spectra obtained from a volunteer were first multiplied with a phase  $e^{-i\theta(k)}$  as determined from the last seven polynomial coefficients and then inversely Fourier transformed into A-lines, thus removing dispersion.

### 3.2 Setup

The turn-key ultra-broadband source was a BroadLighter (Superlum, Russia), in which two super luminescent diodes at center wavelengths of approximately 840 nm and 920 nm were combined in one system with a center wavelength of 890 nm, a FWHM bandwidth of over 150 nm and an optical output power of approximately 4.5 mW. Fig. 1 shows the source spectrum and a reference arm spectrum that were recorded with a commercial optical spectrum analyzer (OSA). The reference spectrum was also recorded with our high-speed spectrometer (HS-OSA). By comparing the blue and red curves of Fig. 1, one can see a significant drop in sensitivity of the line scan camera above 850 nm. The plot amplitudes are adjusted so that all three curves fit within the same graph.

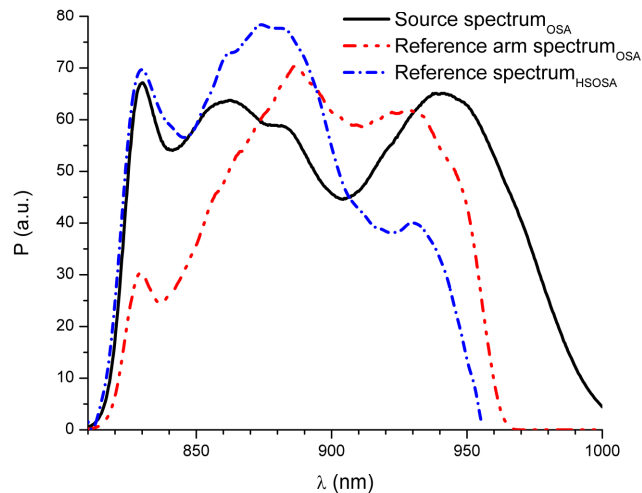


Fig. 1. Source spectrum of the BroadLighter (black); spectrum returning from the reference arm (red). Both spectra were measured with a commercial optical spectrum analyzer. The reference spectrum in blue was recorded with our high-speed spectrometer, and by comparing the blue and red line it demonstrates the decrease in sensitivity of the line scan camera above 850 nm. Spectrum amplitudes were adjusted so that all three curves fit within the same graph.

A detailed description and drawing of our setup can be found in our earlier work. [18, 20] Back reflected light from the source was isolated with a broadband isolator. Without the isolator, back reflections induce noise in the OCT system. After isolation, the power was split with a fiber coupler. The splitting ratio of this coupler was optimized to 80/20 at 830 nm. At

longer wavelengths, the splitting ratio approaches 50/50. The manufacturer specification (Gould Fiber Optics, Millersville, MD) of wavelength dependent shift in splitting ratio is 0.3%/nm. The larger fraction was sent towards a stationary rapid scanning optical delay line, in which the lens-to-grating distance was optimized to minimize group-delay or second order dispersion. The smaller fraction of the power was sent towards the sample arm, where a slit lamp-based scanner apparatus was available for retinal scanning. [10] Previously, we used a dichroic splitter in the slit lamp, so that the location of scans could be monitored by a charged coupled device (CCD) camera. In order to reduce the losses in the slit lamp, this dichroic mirror was replaced by a gold mirror. After this replacement, the total attenuation in the slit lamp was 1 dB in single pass. Longer wavelengths were blocked with a short-pass filter with a cut-off wavelength of 950 nm. The power that was incident on the cornea after low-pass filtering was equal to  $395 \pm 5 \mu\text{W}$ . This power is well below the allowed maximum for scanning beams as specified by the ANSI standards. [7] Power returning from the eye and the reference arm interfered in the 80/20 fiber coupler. Interference fringes were detected with a high-speed spectrometer, comprising a collimator ( $f = 60 \text{ mm}$ ), a transmission grating (1200 lines/mm) at Littrow's angle, a three-element air-spaced focusing lens ( $f = 100 \text{ mm}$ ) and a line scan camera (Basler) with 2048 elements (each  $10 \mu\text{m} \times 10 \mu\text{m}$ ). The bandwidth of the spectrometer was 145 nm, with a designed spectral resolution equal to 0.071 nm. [18, 20] The maximum scan depth  $z$  was measured to be equal to 2.7 mm in air and 2.0 mm in tissue ( $n = 1.38$ ). The galvanometer's mirror in the delay line was set in a neutral position and was not driven for these measurements. Since the source bandwidth was larger than the bandwidth of the spectrometer, the spectrum was clipped at one side by offsetting the reference arm mirror such that longer wavelengths were not reflected back into the interferometer. The reference arm power was adjusted with a neutral density filter in the delay line. In the spectrometer, consecutive interference spectra were read out using a custom-made program written in Visual C++. [18, 20] Data was stored on a hard disk. The continuous acquisition rate was 29,300 spectra per second. The integration time per spectrum was equal to 34  $\mu\text{s}$ . The duty cycle was 98%, i.e. data was acquired during 98% of the total imaging time.

### 3.3 Measurement procedure

In order to compensate for dispersion, coherence functions were obtained from a reflecting spot in the foveal umbo of a human eye, from a mirror in a water-filled model eye (Eyetechn Ltd.) and a mirror in air. The sensitivity of the OCT system and determination of depth-dependent dispersion were tested with use of a mirror. The slit lamp setup was not used for this particular measurement. Instead, a collimator, a focusing lens and a mirror on a translation stage were used. In order to extrapolate the results to the slit lamp experiments, a low pass filter ( $\lambda_{\text{cut-off}} = 950 \text{ nm}$ ) was inserted in the beam path. The sample arm power could be attenuated with a variable neutral density filter. To verify that the system was free from any depth-dependent dispersion induced by the spectrometer, the reference arm length was changed and measurements were taken at different positions. The depth-dependent attenuation was measured as well. In order to determine whether the system was shot noise limited, the variance of 1000 reference arm spectra was determined, and fit with a theoretical expression for the shot noise. [20]

*In vivo* measurements were performed on the undilated right eye of a healthy volunteer. The right eye was stabilized using an external fixation spot for the volunteer's colateral eye. Multiple sets of B-scans were taken in the macular area at an acquisition rate of 29,300 spectra per second. During acquisition, a refresh rate on screen of three frames per second without dispersion compensation was maintained. For each frame the fast axis of the retinal scanner was deflected once, while the slow axis of the scanner could be stepped between frames. B-scans that contain specular reflections from the foveal surface were analyzed in detail to compensate for dispersion.

### 3.4 Analysis

Data was analyzed after acquisition with a custom-made program written in Matlab. Raw data was processed in several steps to extract structural intensity images [18, 20, 26] as well as Doppler flow data. [27] In addition, we compensated for dispersion using a phase  $e^{-i\theta(k)}$ , built with a set of polynomial coefficients  $\alpha_{3,9}$  obtained from a specular reflection in the human retina. For the coherence length determination, the density of points within an A-line was increased eightfold by zero-padding the spectral data. [26] For all data obtained from a mirror, we averaged over 100 A-lines to reduce the influence of noise. The dispersion analysis in software, which required input from the operator, took approximately five minutes in Matlab. Raw data was converted to movies in Matlab as well. To improve sensitivity, two consecutive spectra were summed before Fourier transformation. At an effective A-line rate of 14,600 per second and an effective integration time of 68  $\mu\text{s}$  per spectrum, movies of 500 A-lines per frame were created. The conversion from a data set acquired in 3 seconds into a movie took approximately twenty minutes in MatLab.

## 4. Results

### 4.1 Dispersion compensation

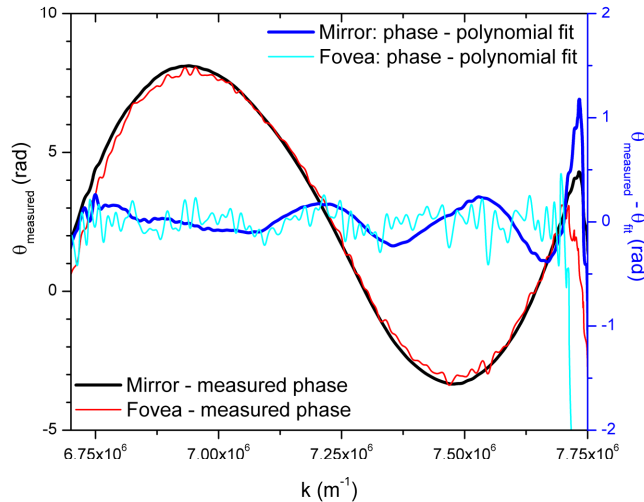


Fig. 2. The phase  $\theta(k)$  obtained from a mirror in a model eye and from a specular reflection in the fovea (left axis). The residual dispersion not compensated for by the polynomial fit is given as a function of  $k$  (right axis).

In the graph of Fig. 2, the phase term  $\theta(k)$  obtained from a mirror in a model eye (averaged over 100 A-lines) and from a specular reflective spot in the fovea (averaged over 5 A-lines) are shown. The differences between the measured phase terms and polynomial fits (9<sup>th</sup> order) to the data are shown as well, with the corresponding axis on the right. The inclusion of more than 9 coefficients in the polynomial fit did not significantly improve the coherence function. Both phases show the same pattern, which indicates that both the model eye and the real eye experience similar amounts of dispersion. All *in vivo* data was compensated using the phase that was obtained from the specular reflection of the fovea itself (red curve of Fig. 2).

In the graph of Fig. 3, the coherence function obtained from a mirror in air is plotted. The data shows the amplitude as a function of depth, where the amplitude is given by the absolute value of the Fourier components after transform of the measured spectrum. In the same graph, a coherence function compensated for dispersion is plotted. For this plot, the same technique

as applied in Fig. 2 was used, yielding a different set of coefficients, since the mirror was not located in the water-filled model eye.

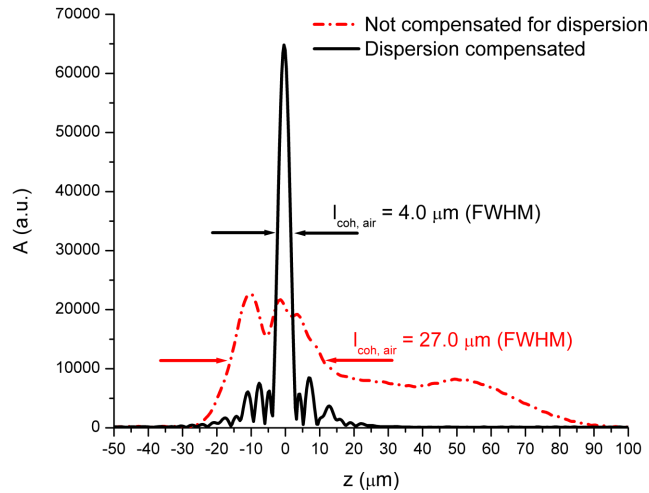


Fig. 3. Coherence function obtained from a mirror in air. Uncompensated data (red) is compared with a coherence function after dispersion compensation (black). The density of points was increased by a factor of 8 using a zero-padding technique.

The dispersion compensation technique gives a significant reduction in coherence length as well as a threefold increase in peak height. Without dispersion compensation, the coherence length was 27.0  $\mu\text{m}$ . After dispersion compensation it was estimated to be 4.0  $\mu\text{m}$  ( $n = 1$ ), equivalent to 2.9  $\mu\text{m}$  in tissue with a refractive index of  $n = 1.38$ . After dispersion compensation, side lobes are present at both sides of the coherence function. These side lobes are a result of the non-Gaussian shaped reference arm spectrum (Fig. 1).

In Fig. 4, coherence functions obtained from a mirror in air at different path length differences are plotted. The coherence function plotted in black was dispersion compensated, using the earlier mentioned dispersion compensation technique. This process yielded a dispersion compensation phase  $e^{-i\theta(k)}$ . All other data sets were multiplied with the same phase before Fourier transformation. Coherence functions from different depths were overlapped for comparison. The point density of all curves was increased by a factor of 8, using zero padding. The coherence length for path length differences up to 1200  $\mu\text{m}$  was 4.0  $\mu\text{m}$  in air. At  $z = 1700 \mu\text{m}$ , the coherence length increased to 4.1  $\mu\text{m}$  and at  $z = 2200 \mu\text{m}$  it further increased to 4.3  $\mu\text{m}$ .



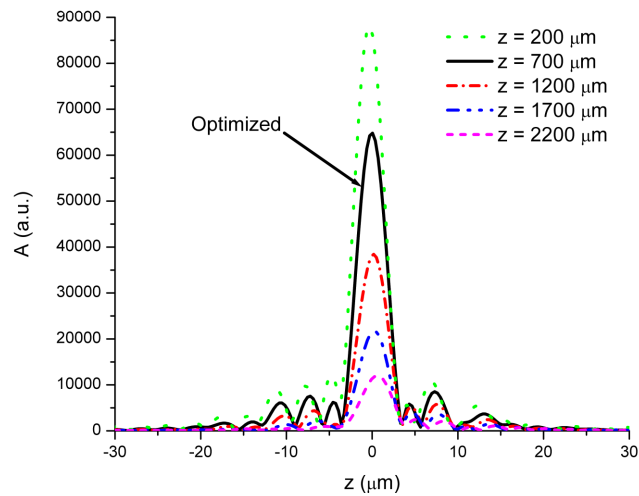


Fig. 4. Coherence functions obtained from a mirror at different path length differences  $z$ . The coherence function at  $z = 700 \mu\text{m}$  was dispersion compensated, and the data of all other curves was multiplied with the same phase  $e^{-i\theta(k)}$  before Fourier transformation. The coherence length for path length differences up to  $1200 \mu\text{m}$  was  $4.0 \mu\text{m}$  in air,  $4.1 \mu\text{m}$  for  $z = 1700 \mu\text{m}$  and  $4.3 \mu\text{m}$  for  $z = 2200 \mu\text{m}$ .

The depth dependent attenuation was calculated from Fig. 4, [20] comparing peaks at  $z = 200$  and  $1200 \mu\text{m}$  and found to be equal to  $7.2 \text{ dB}$ .

#### 4.2 Noise performance

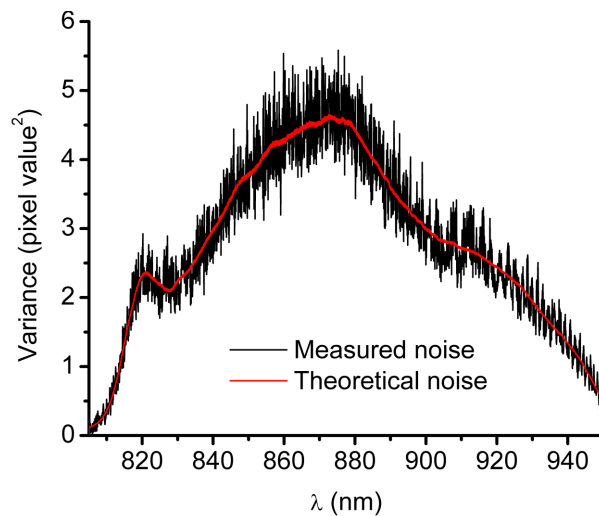


Fig. 5. Shot noise measurement using the BroadLighter in an SD-OCT configuration. The shot noise level was determined with illumination of the reference arm only. The measured shot noise curve was fit with a theoretical equation of the shot noise, demonstrating that the system was shot noise limited. [20]

An analysis on 1000 reference spectra demonstrated that the system was shot noise limited, using the same method and well depth as in Ref. [20]. An isolator in the source arm was required to suppress optical feedback to the source.

#### 4.3 Sensitivity measurements

The maximum power after the sample arm fiber collimator was 533  $\mu\text{W}$ . Using a mirror in the sample arm, 101  $\mu\text{W}$  returned to the detector arm. After attenuation with a 30.8 dB neutral density filter in the sample arm, 83.7 nW was detected at the detection arm, and a signal to noise ratio (SNR) of 58.0 dB was measured with our high-speed spectrometer at an acquisition rate of 29,300 spectra per second (see coherence function at  $z = 700 \mu\text{m}$ ). In theory, a detected power of 83.7 nW with our earlier reported spectrometer efficiency of 28% should give an SNR of 65.6 dB. [20] Comparing this value with the measured value of 58.0 dB, the spectrometer performed 7.6 dB below the theoretical SNR. The reduction is attributed to a reduced quantum efficiency of the detector for longer wavelengths. For a measured 400  $\mu\text{W}$  sample arm power after the slit lamp, a return loss through the slit lamp of 1 dB and a 3 dB sensitivity gain by coherent addition of two consecutive spectra, the system sensitivity was 89.6 dB at a 14,600 A-lines/sec acquisition rate.

#### 4.4 In vivo measurements on a human volunteer

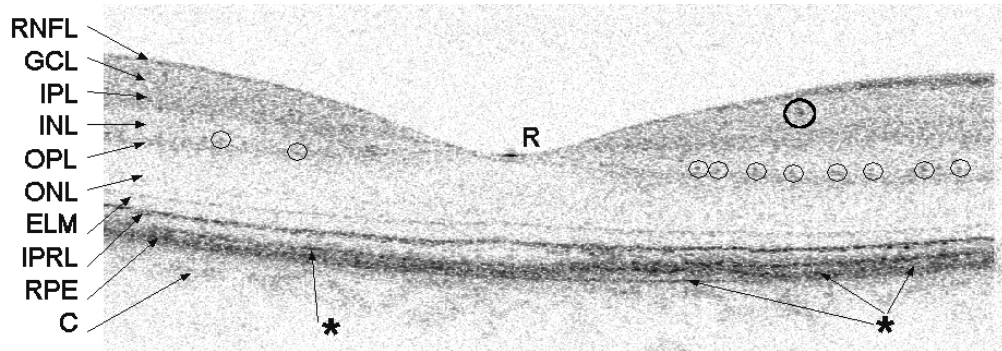


Fig. 6. Structural image of the fovea. The dimensions of each image are 3.1 x 0.61 mm. The image is expanded in vertical direction by a factor of 2 for clarity. Layers are labeled as follows: RNFL – retinal nerve fiber layer; GCL – ganglion cell layer; IPL – inner plexiform layer; INL – inner nuclear layer; OPL – outer plexiform layer; ONL – outer nuclear layer; ELM – external limiting membrane; IPRL – interface between the inner and outer segments of the photoreceptor layer; RPE – retinal pigmented epithelium; C – choriocapillaris and choroid. A highly reflective spot in the center of the fovea is marked with an R. A blood vessel is marked with a large circle (BV) and structures in the outer plexiform layer are marked with smaller circles. In the movie, these structures can also be seen in the IPL. Two layers at the location of the RPE at the left and right are marked with arrows and an asterisk (\*). Click on the image to view the movie (29.3 frames per second and 500 A-lines per frame, aspect ratio 1:3.2, short version 45 frames (1.5 s, 2.4 MB), long version 90 frames (3.1 s, 5.3 MB). In the movie, a floater can be seen in the vitreous at the left hand side above the retina. The repositioning of the galvo mirror after each scan creates an artifact in the image on the right hand side.

The movie in Fig. 6 was recorded in the fovea at an acquisition rate of 29.3 frames per second with 500 A-lines per frame. The movie is expanded in vertical direction by a factor 3.2. The retinal scanner made horizontal scans through the fovea. For this particular movie, the slow axis of the retinal scanner was not run and as a result cross-sections from approximately the same location can be seen as a function of time. Individual frames in the movie were realigned using a cross-correlation technique to remove motion across frames. The dimensions

of each image are 3.1 x 0.6 mm. A depth range between 0.4 and 1.0 mm is displayed in the images. The maximum dynamic range within the image was equal to approximately 35 dB. Several layers can be recognized in this movie. [5] The upper dark band at the left and right of the image is the retinal nerve fiber layer that becomes thicker further away from the fovea. Below this layer, we see two dark bands delineated by two whiter bands. The upper dark band consists of the ganglion cell layer and the inner plexiform layer. In several frames, one may be able to distinguish between these two layers. The two white bands are the inner and outer nuclear layers, and the second dark band is the outer plexiform layer. The first dark layer below the outer nuclear layer is the external limiting membrane, which extends over the whole width of the image. This layer is in general not visible with OCT employed with an ordinary broadband source. Below this membrane we can see the interface between the inner and outer segments of the photoreceptor layer, which rises directly below the foveola. The lowest layer comprises the retinal-pigmented epithelium (RPE). At the left and right side of the image at the location of the RPE, two layers seem to be present. We hypothesize that one of these layers might be Bruch's membrane. Below the RPE, a cloudy structure can be seen. This structure is the choriocapillaris and the choroid. The fast acquisition rate reveals the true topography of the retina. The coherence length was determined *in vivo* from the specular reflection in the center of the fovea, averaged over 5 A-lines. This coherence function is plot in Fig. 7, and the coherence length after dispersion compensation was equal to 4.8  $\mu\text{m}$  in air and 3.5  $\mu\text{m}$  in tissue ( $n = 1.38$ ). Compared to the coherence length displayed in Fig. 3, using the same index of refraction of 1.38, the coherence function is broadened. Due to absorption of longer wavelengths in the vitreous, the effective bandwidth is reduced, yielding a longer coherence length.

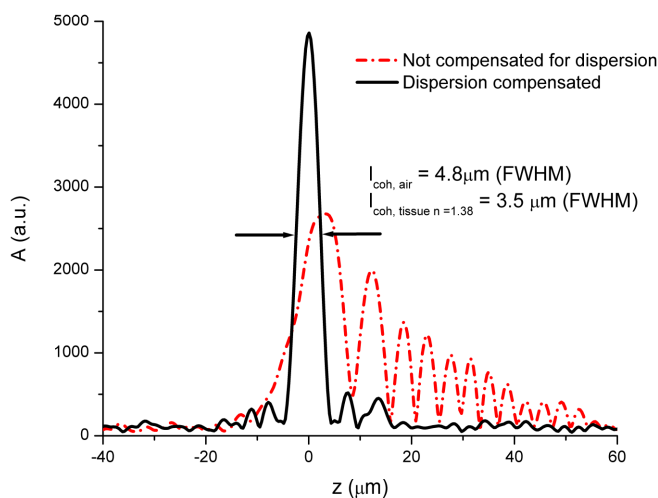


Fig. 7. Coherence function obtained from a reflective spot in the fovea. The coherence length is equal to 4.8 $\mu\text{m}$  in air.

Small highly-reflecting black dots can be seen in the ganglion cell layer and in both plexiform layers. We conclude that they are not caused by speckle, because they consistently appear at the same location over consecutive movie frames. The dots seem to be almost regularly spaced in the outer plexiform layer. We believe that these black dots are very small blood vessels. Snodderly *et al* measured the distribution of blood vessels in an enucleated macaque eye by means of microscopy in frozen samples. [28] They report a very similar spacing of small blood vessels in the plexiform layers near the fovea. To positively identify these structures as blood vessels, we analyzed the data for blood flow as described in our earlier

work. [27] Doppler flow analysis confirmed that flow occurs in the darker dots located in the ganglion cell layer, which therefore can be positively identified as blood vessels. In the plexiform layers, a clear correlation between location of the highly reflective black dots and Doppler flow could not be found. Flow was only detected incidentally in these layers at locations where black dots were seen. One explanation that no consistent flow was detected in the well-reflecting features in the plexiform layers is that these features are not blood vessels. Another explanation may be that our system is not sensitive enough to measure flow in such small vessels. For instance, the blood vessels may be too small, which reduces the number of A-lines and therefore the signal that can be used to determine the presence of blood flow. Furthermore, the analysis depends on measuring a Doppler component parallel to the direction of the beam. If the blood vessel is exactly perpendicular to the beam direction, a parallel Doppler flow component will be absent and no flow can be registered. In previous work, larger blood vessels were recognized by their white appearance and the shadow they cast, caused by light attenuation in the blood. Here blood vessels act as good scatterers, presumably due to their small sizes.

By running the slow axis of the retina scanner, subsequent cross sections of the fovea were made. The image below measures 6.2 by 1.2 mm and the slow axis scans over 3.1 mm. During processing, noise was filtered with a 2 by 2 median filter to match the data better to the pixel resolution of this video.

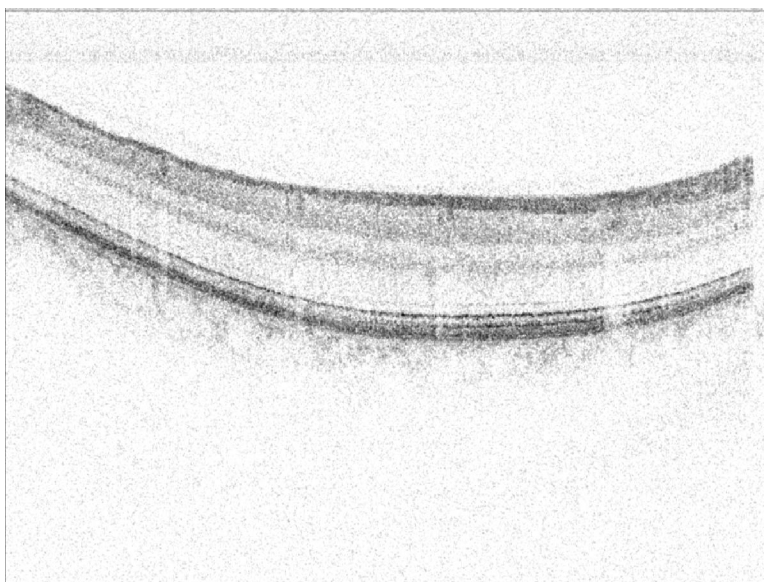


Fig. 8. Structural image of the fovea. The dimensions of each image are 6.2 x 1.2 mm. The slow axis in the movie scans over 3.1 mm. Click on the image to view the movie (2.4 s, 45 frames, with 29.3 frames per second and 500 A-lines per frame, 2.3 MB).

The reflecting spot in the center of the foveola, as seen in the first movie, only shows up in a couple of frames, indicating that the specular reflection only occurs in the three-dimensional center of the foveola. The horizontal lines at the top of the image are residual fixed pattern noise. Summarizing the previous, the application of ultrahigh-resolution SD-OCT technology allows us to identify new features in the human retina and measure the coherence length in the eye.

## 5. Discussion

In this study, the performance of an SD-OCT system equipped with an ultra-broadband source was determined by measuring the SNR and the coherence length on a mirror and in the eye. Comparing the measured SNR value of 89.6 dB with the theoretical value of 97.2 dB, our system performs 7.6 dB below the theoretical limit. In our previous system described by Nassif *et al*, the difference between the measured and theoretical SNR was 2.2 dB. [20] The extra loss of 5.4 dB that we encounter in this system equipped with the BroadLighter can be attributed to the lower sensitivity of the line scan camera. In Fig. 1, the reference arm spectrum recorded with a commercial optical spectrum analyzer is compared with the same spectrum as recorded with our high-speed spectrometer. The sensitivity of our line scan camera drops by at least a factor of two above 850 nm.

In a conventional HR-OCT system, the highest documented A-line rate is equal to 250 A-lines per second. The power incident on the cornea was equal to 500-800  $\mu\text{W}$ , resulting in a sensitivity of 95 dB. The A-line length was equal to 1-2.8 mm. [5] The effective A-line rate of our SD-OCT system was 14,800 A-lines per second, and the measured sensitivity was 89.6 dB, with a power of  $395 \pm 5 \mu\text{W}$  incident on the cornea. Comparing the two systems, the spectral-domain OCT system was 59 times faster at a 5.4 dB lower sensitivity.

## 6. Conclusion

The axial resolution of a TD-OCT system increases with bandwidth, but its SNR is inversely proportional to an increase in bandwidth. Since source bandwidth does not affect the SNR performance of a SD-OCT configuration, SD-OCT is preferred for ultrahigh-resolution ophthalmic imaging. However, ultra-broadband sources induce more dispersion than standard broadband sources. With dispersion compensation in software, we managed to reduce dispersion artifacts significantly. After dispersion compensation, the coherence length measured from a mirror in air was equal to  $4.0 \mu\text{m}$  ( $n = 1$ ). The dispersion-compensated axial resolution obtained from a reflecting spot in the fovea was equal to  $3.5 \mu\text{m}$  ( $n = 1.38$ ). To our knowledge, this is the first coherence length measured in the human eye *in vivo*. The combination of high axial resolution measurements at a high data acquisition rate allows us to identify features that have not been seen in the human retina before with OCT. Movies at 29.3 frames per second with 500 A-lines per frame seem to indicate two layers at the location of the RPE as well as not earlier seen small structures in the two plexiform layers, which determined from their location are believed to be blood vessels. Comparing the performance of our ultrahigh-resolution SD-OCT system with a conventional high-resolution time domain OCT system, the A-line rate of the spectral-domain OCT system was 59 times higher at a 5.4 dB lower sensitivity.

## Acknowledgments

This research was supported in part by a research grant from the National Institutes of Health (1R24 EY12877). Research grants for technical development were provided in part by the National Institute of Health (R01 EY014975 and RR19768), Department of Defense (F4 9620-01-1-0014), CIMIT, and a gift from Dr. and Mrs. J.S. Chen to the optical diagnostics program of the Wellman Center of Photomedicine.